Research Square

Preprints are preliminary reports that have not undergone peer review.
They should not be considered conclusive, used to inform clinical practice,
or referenced by the media as validated information.

Kinematics and excitation of ionized gas in the stellar counterrotating galaxies PGC 35706 and LEDA 2220522

V. S. Goradzhanov

vgoradzanov@gmail.com

Lomonosov Moscow State University

K. O. Parfenov

P.N. Lebedev Physical Institute of the Russian Academy of Sciences

D. Gasymov

Zentrum für Astronomie der Universität Heidelberg

Research Article

Keywords:

Posted Date: October 29th, 2026

DOI: https://doi.org/10.21203/rs.3.rs-11267702/v1

License: This work is licensed under a Creative Commons Attribution 4.0 International License.
Read Full License

Additional Declarations: No competing interests reported.

Kinematics and excitation of ionized gas in the stellar counterrotating galaxies PGC 35706 and LEDA 2220522

V. S. Goradzhanov[1,2*], K. O. Parfenov[3] and D. Gasymov[4,1]

[1*]Sternberg Astronomical Institute, Lomonosov Moscow State University, Moscow, 119234, Russia.
[2]Faculty of Physics, Lomonosov Moscow State University, Moscow, 119991, Russia.
[3]Astro Space Center, P. N. Lebedev Physical Institute of the Russian Academy of Sciences, Moscow, Russia.
[4]Astronomisches Rechen-Institut, Zentrum für Astronomie der Universität Heidelberg, Heidelberg, Germany.

*Corresponding author(s). E-mail(s): vgoradzanov@gmail.com;

Abstract

We compare the kinematics and excitation of ionized gas in the stellar counterrotating galaxies PGC 35706 and LEDA 2220522. We assess the regularity of gas rotation using an axisymmetric model, two spectral analyses of the same observations, and emission-line diagnostics. The stellar and gas velocity gradients are nearly opposite in both galaxies, but the gas properties differ. In LEDA 2220522, the root-mean-square residual of the gas model is 5.90 $\mathbf{km\,s^{-1}}$. The two analyses agree in both the gradient direction and local velocities, supporting regular gas counterrotation. In PGC 35706, structured residuals have a root-mean-square value of 45.5 $\mathbf{km\,s^{-1}}$, dominated by a few bins with extreme velocities. Agreement between the two analyses is substantially poorer at the level of local velocities. Excitation diagnostics identify regions consistent with star formation in LEDA 2220522. In PGC 35706, weak, low-ionization emission provides no basis for estimating the star formation rate from H$\boldsymbol{\alpha}$. Interpreting gas counterrotation therefore requires separate assessments of the velocity-gradient direction, the regularity of the velocity field, and gas excitation.

Keywords: galaxies: individual: PGC 35706, LEDA 2220522; galaxies: kinematics and dynamics; galaxies: interstellar medium; galaxies: stellar populations

1 Introduction

Galaxies with counterrotating stellar components provide a means of studying the formation of kinematically distinct structures. Such components occur in both disc and early-type galaxies (Rubin et al. 1992; Rix et al. 1992; Coccato et al. 2011; Johnston et al. 2013). Their stellar populations, relative contributions, and spatial structures vary considerably (Coccato et al. 2013; Katkov et al. 2013, 2016; Coccato et al. 2015; Morelli et al. 2017); stellar counterrotation therefore does not identify a unique formation scenario.

Proposed mechanisms include the accretion of gas with oppositely directed angular momentum followed by star formation, mergers, and internal orbital redistribution (Thakar and Ryden 1996; Algorry et al. 2014; Martel and Richard 2020; Starkenburg et al. 2019; Khoperskov et al. 2021; Bugueño et al. 2026).

Integral-field spectroscopic surveys show that stellar–gas kinematic misalignment occurs across a range of gas-field asymmetries, metallicities, excitation conditions, and star formation properties (Davis et al. 2011; Ristea et al. 2022; Zhou et al. 2022; Zinchenko 2023; Beom et al. 2024; Tous et al. 2026). Emission-line ratios and equivalent widths provide spatially resolved diagnostics of gas excitation (Belfiore et al. 2016; Zhang et al. 2017; Lacerda et al. 2018).

For galaxies with stellar counterrotation, it is particularly important to distinguish a candidate selected by the difference in kinematic position angles, accounting for the direction of the velocity gradient, from a regularly rotating gas disc. MaNGA catalogues include cases with weak, irregular, or undetected gas, whereas samples of regular counterrotating gas discs explicitly exclude such cases (Bevacqua et al. 2022; Gasymov et al. 2025; Bao et al. 2022, 2026). Detailed studies of individual objects also combine stellar-component decomposition or orbit modelling with gas kinematics (Bao et al. 2024). We examine whether gas motion opposite to the stars corresponds to regular disc rotation. To this end, we quantify departures of the gas velocities from an axisymmetric model, compare two spectral analyses, and investigate gas excitation using emission-line ratios.

The galaxies PGC 35706 and LEDA 2220522 and their earlier Schwarzschild decomposition are presented by Goradzhanov et al. (2026a). The observed stellar and gas velocities are taken from that work. To compare the gas with orbital families, we use models from a study of the stellar populations of these galaxies (Goradzhanov et al. 2026b); their assumptions are outlined in Sect. 2.4.

2 Data and models

2.1 Targets

Table 1 lists the target parameters adopted from the published dynamical analysis. Distances, spatial scales, inclinations, and effective radii are fixed; Hα luminosities are calculated using $D_L = D_A(1+z)^2$.

Table 1 Adopted target parameters.

Parameter	PGC 35706	LEDA 2220522
MaNGA plate–IFU	8992–3704	8254–1902
z (MaNGA)	0.0261	0.0242
D_A (Mpc)	117.5	108.6
D_L (Mpc)	123.7	114.0
Scale (kpc arcsec^{-1})	0.570	0.527
Inclination (deg)	42	27
z-band MGE R_e (arcsec; kpc)	3.48; 1.98	2.52; 1.33

The targets were selected for the preceding analysis of two stellar components. Legacy Surveys images (Dey et al. 2019) show no obvious strong distortions.

2.2 Spectral measurements of ionized gas

The primary measurements of velocities, emission-line fluxes, and equivalent widths were obtained with NBursts from MaNGA DR17 observations (Smee et al. 2013; Blanton et al. 2017; Abdurro'uf et al. 2022; Goradzhanov et al. 2026a). The spectra are combined into 676 Voronoi bins for PGC and 263 for LEDA. The stellar continuum and emission lines are fitted simultaneously, with independent stellar and gas kinematics; the emission is described by a Gauss–Hermite profile. The analysis includes Hβ, [O III]λ5007, [O I]λ6300, Hα, [N II]λ6584, and the [S II] doublet. Where a tabulated [O I] flux is unavailable, it is estimated from the spectrum (Appendix A.2).

Fluxes are expressed as the integral of the line model over observed wavelength and corrected for Milky Way extinction following O'Donnell (1994), with $R_V = 3.1$ and $E(B-V) = 0.01269$ for PGC and 0.01651 for LEDA. Equivalent widths are given in the rest frame throughout. Fluxes refer to entire spectral bins; the maps show surface brightness.

We assess the dependence of the measurements on spectral processing by comparison with MaNGA Data Analysis Pipeline (DAP; Westfall et al. 2019; Belfiore et al. 2019) results for the same observations. We characterize the Hα line width by the DAP Gaussian dispersion corrected for instrumental broadening: $\sigma_{\rm corr} = (\sigma^2_{\rm DAP} - \sigma^2_{\rm inst})^{1/2}$. The data reduction and point spread function (PSF) are described by Law et al. (2016).

2.3 Stellar and gas kinematics from NBursts

The gas and stellar line-of-sight velocity fields are taken from the NBursts spectral analysis (Goradzhanov et al. 2026a). Both fields are measured on the same Voronoi tessellation, allowing a direct comparison of gas and stellar kinematics. We use bins with valid Hα fits and $S/N(\mathrm{H}\alpha) \geq 5$. For comparison, DAP H$\alpha$ velocities are flux-weighted within the same bins over the common spatial coverage.

2.4 Stellar dynamical models

The axisymmetric Schwarzschild solutions used to compare orbital families are taken from Goradzhanov et al. (2026b) and were constructed with Forstand (Vasiliev and

Valluri 2020) and AGAMA (Vasiliev 2019). They use a multi-Gaussian expansion (MGE) of the z-band surface brightness, an isothermal halo with core radius $r_{\rm core} = R_{\rm e}$, and a radially varying stellar mass-to-light ratio. Orbit weights were fitted to the stellar density and four kinematic moments (V, σ, h_3, and h_4), with regularization. Gas data were not included in the fit. Projected orbital-family velocities are calculated from the line-of-sight velocity distributions in the observed Voronoi bins.

3 Methods

3.1 Gas excitation, oxygen abundance, and star formation

We assess excitation using Baldwin–Phillips–Terlevich line-ratio diagrams (BPT; Baldwin et al. 1981) and the WHAN equivalent-width diagram (Cid Fernandes et al. 2011). The primary [N II]-BPT classification requires $S/N \geq 3$ in Hβ, [O III], Hα, and [N II], with boundaries from Kauffmann et al. (2003) and Kewley et al. (2001). The WHAN diagram uses [N II]/Hα and EW(Hα). Its strong and weak active galactic nucleus sectors are denoted sAGN and wAGN. Measurement errors are propagated for diagnostics involving the weak [S II] and [O I] lines (Kewley et al. 2001, 2006) and for probabilistic WHAN maps; a class is displayed only when its probability is at least 0.8. Classification rules, error assumptions, and checks using detected lines are given in Appendix A.2.

The star formation rate (SFR) and gas-phase oxygen abundance are estimated for LEDA. The primary star-forming mask requires $S/N \geq 3$ in Hα and Hβ, $P_{\rm SF}^{\rm [S\,II]} \geq 0.8$, $P_{\rm SF}^{\rm [O\,I]} \geq 0.8$, and EW(Hα) > 6 Å. We use the O3N2 and N2 oxygen-abundance calibrations of Marino et al. (2013) within their calibrated ranges, requiring detections of all four contributing lines. Their calibration scatters are 0.18 and 0.16 dex. Oxygen abundances are derived from line ratios corrected for internal attenuation. This correction is determined from the Balmer decrement, assuming an intrinsic ratio of 2.86 for case B (Hummer and Storey 1987) and the Cardelli et al. (1989) law with $R_V = 3.1$; negative estimates of $E(B-V)$ are set to zero. For a Kroupa initial mass function (Kroupa 2001), we adopt SFR $= 10^{-41.27} L$(Hα) (Kennicutt and Evans 2012).

The SFR refers to the selected region within the MaNGA coverage. Statistical uncertainty is estimated by Monte Carlo sampling with a fixed mask, accounting for spatially correlated errors on the PSF scale. The effects of the attenuation law and the choice of diagnostic region are tested separately (Appendix A.4).

3.2 Comparison of two spectral analyses

NBursts and DAP measurements are compared in identical apertures after matching the flux normalization and Galactic extinction correction. DAP fluxes are summed over the spaxels in each NBursts bin. Each line must have $S/N \geq 3$ in both analyses. The uncertainty in a summed DAP flux is the sum of the uncertainties of its constituent spaxels, corresponding to full correlation within the bin. We characterize the distribution of flux ratios across bins by its median and 16th–84th percentiles.

The effect of spatial binning is tested separately in single-spaxel bins. SFRs are compared over the intersection of regions selected as star-forming by both analyses using identical criteria. DAP processing of the summed NBursts spectra with additional quality cuts is described in Appendix A.3.

3.3 Gas-field regularity and velocity-gradient directions

To assess regularity, we fit each NBursts gas velocity field with an axisymmetric arctangent model:

$$V_{\rm mod} = V_{\rm sys} + \frac{2A}{\pi} \arctan(R/R_t) \sin i \, \frac{X}{R}, \qquad R^2 = X^2 + (Y/\cos i)^2, \tag{1}$$

where $V_{\rm sys}$ is the systemic velocity, A and R_t are the amplitude and radial scale of the rotation curve, and i is the disc inclination. Coordinates X, Y run along the model major and minor axes relative to the fitted centre. The robust fit uses one velocity per Voronoi bin and the inclination in Table 1. The model is evaluated at bin centres without PSF convolution. The error model, fitting procedure, and sensitivity tests are given in Appendix A.1.

To compare large-scale directions independently of this rotation model, we perform a weighted plane fit:

$$V(x, y) = V_0 + ax + by. \tag{2}$$

With the x-axis pointing east and the y-axis north, the angle $\theta_{\rm grad}$ gives the direction of increasing line-of-sight velocity, measured from east towards north over 360 deg. Signed angular differences are reported in $[-180^\circ, 180^\circ)$, preserving the distinction between opposite gradients. Uncertainties are estimated using a joint spatial block bootstrap.

Comparison with DAP tests whether the gradient direction and local gas velocities are reproduced by a different spectral-fitting procedure. The NBursts and DAP gas velocity fields are compared on common Voronoi bins. After subtracting the median of each field, we calculate the unweighted Pearson correlation coefficient and the root-mean-square velocity difference, without fitting a relative scale factor.

3.4 Projected orbital-family velocity fields

For the kinematic comparison, we use broad retrograde and prograde orbital families:

$$-1 \le \lambda_z < -0.35, \qquad +0.35 \le \lambda_z \le +1, \tag{3}$$

where $\lambda_z = \overline{L_z}/L_{\rm circ}(E)$ is orbital circularity: the ratio of the time-averaged angular momentum along the symmetry axis to that of a circular orbit of the same energy. The projected and observed fields are compared using velocity-gradient directions and Pearson correlations after subtracting a constant velocity.

4 Results

4.1 Contrasting states of ionized gas

The Hα maps show weak emission relative to the continuum and broad lines in PGC. LEDA contains extended regions with large $EW(\mathrm{H}\alpha)$ and narrower lines (Fig. 1).

None of the 369 PGC bins in the [N II]-BPT sample belongs to the star-forming class; all lie in the retired sector of the WHAN diagram, with a median $EW(\mathrm{H}\alpha) = 0.96$ Å (Table 2). The expected fraction of bins in the low-ionization emission-line region (LIER) class on [S II]-BPT is 92.7 per cent. The [O I]-BPT classification is less constraining because of the low signal-to-noise ratio of this line (Figs. 2, 3). The small equivalent width and absence of star-forming bins on [N II]-BPT provide no basis for applying the adopted SFR and O/H calibrations to PGC.

Among the 385 PGC bins with $S/N \geq 3$ in both Balmer lines, the median Hα/Hβ is 2.63, with a spatial 16th–84th percentile range of 2.31–3.26.

In LEDA, 66.7 per cent of the 231 [N II]-BPT bins are star-forming and 32.9 per cent are composite; the median $EW(\mathrm{H}\alpha)$ is 15.8 Å. Star-forming bins occupy 45.0 per cent of the area: fractions by bin count and by area differ because of adaptive binning. The BPT and WHAN classifications disagree in LEDA: most bins in the star-forming sector of [N II]-BPT lie in the sAGN sector of WHAN.

Table 2 Joint NBursts [N II]-BPT and WHAN classification on a common mask requiring $S/N \geq 3$ in Hβ, [O III], Hα, and [N II]. Bin fractions are calculated for 369 PGC bins and 231 LEDA bins; brackets give the 16th and 84th percentiles of a spatial bootstrap. The final column gives the area fraction for the same sample.

Target	[N II]-BPT / WHAN	N; bin fraction (%)	Area (%)
PGC	composite / retired	14; 3.8 [2.2–5.5]	5.1
PGC	above composite / retired	355; 96.2 [94.5–97.8]	94.9
LEDA	star-forming / SF	22; 9.5 [4.4–13.8]	6.3
LEDA	star-forming / sAGN	132; 57.1 [48.4–64.2]	38.7
LEDA	composite / wAGN	26; 11.3 [7.9–15.7]	29.3
LEDA	composite / sAGN	50; 21.6 [16.4–27.8]	23.9
LEDA	above composite / wAGN	1; 0.4 [0.0–0.9]	1.7

In LEDA, the median oxygen abundance across bins in the primary mask is $12 + \log(\mathrm{O/H}) = 8.62$ for O3N2 and 8.59 for N2, based on 203 and 195 measurements within the calibrated ranges, respectively. Additional mask restrictions shift the medians by less than the calibration scatter of 0.16–0.18 dex (Appendix A.4).

Within the primary mask of 203 bins covering 60.25 square arcseconds, the attenuation-corrected SFR of LEDA is 1.124 $M_\odot\,\mathrm{yr}^{-1}$; the statistical 16th–84th percentile interval is 1.111–1.142 $M_\odot\,\mathrm{yr}^{-1}$. Changing the attenuation law over the same region gives 0.898–1.508 $M_\odot\,\mathrm{yr}^{-1}$.

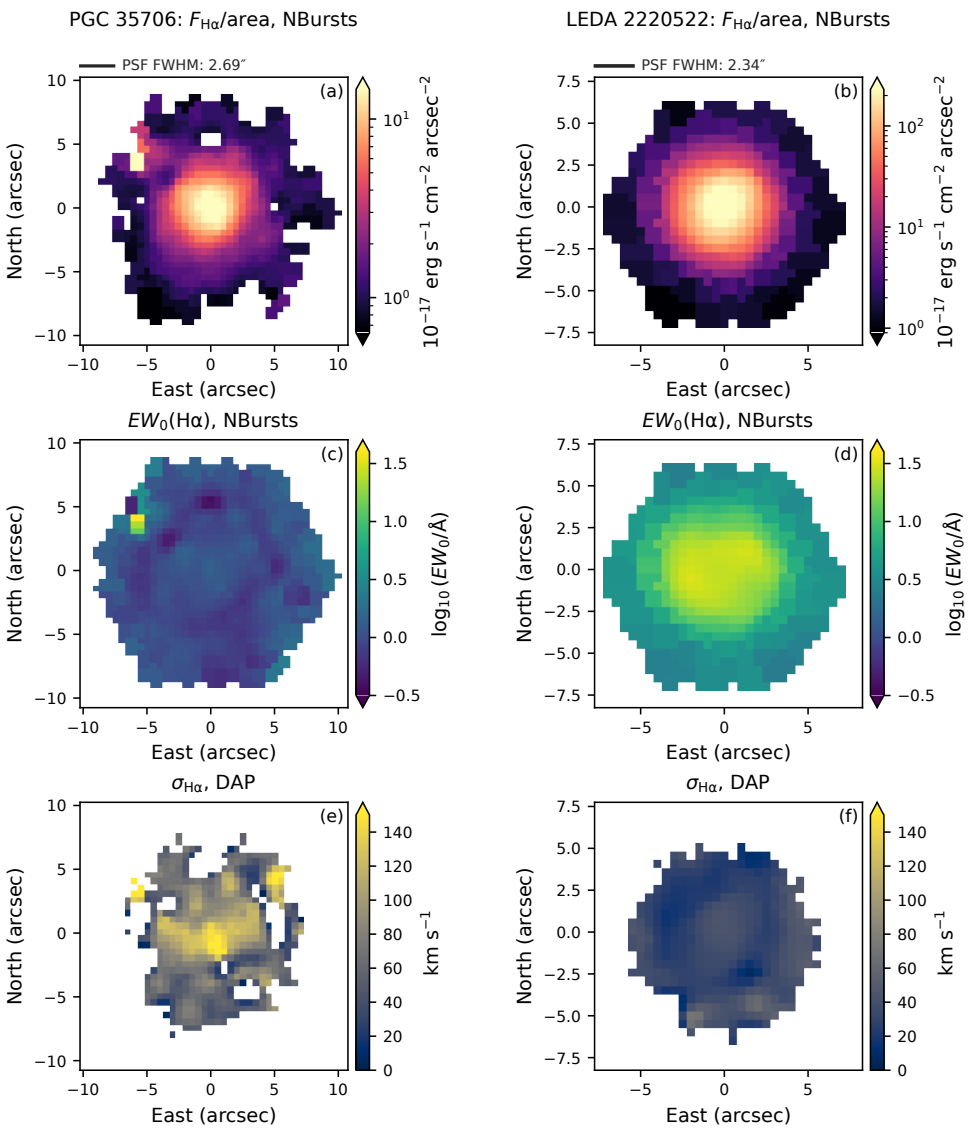


Figure 1 Ionized-gas maps of PGC 35706 (left column) and LEDA 2220522 (right column): NBursts Hα surface brightness (a,b), NBursts $\log_{10}[EW_0(\text{H}\alpha)/\text{Å}]$ (c,d), and DAP Hα dispersion corrected for instrumental broadening (e,f). Broadening due to spatially unresolved velocity gradients has not been removed. Flux maps require $S/N(\text{H}\alpha) \geq 5$; dispersion maps additionally require a positive squared dispersion after the instrumental correction. Panels (c,d) show positive rest-frame equivalent widths. White regions are masked. The surface-brightness scales differ between the two galaxies. Bars above panels (a,b) show the spatial resolution (PSF FWHM): 2.69 and 2.34 arcsec, respectively.

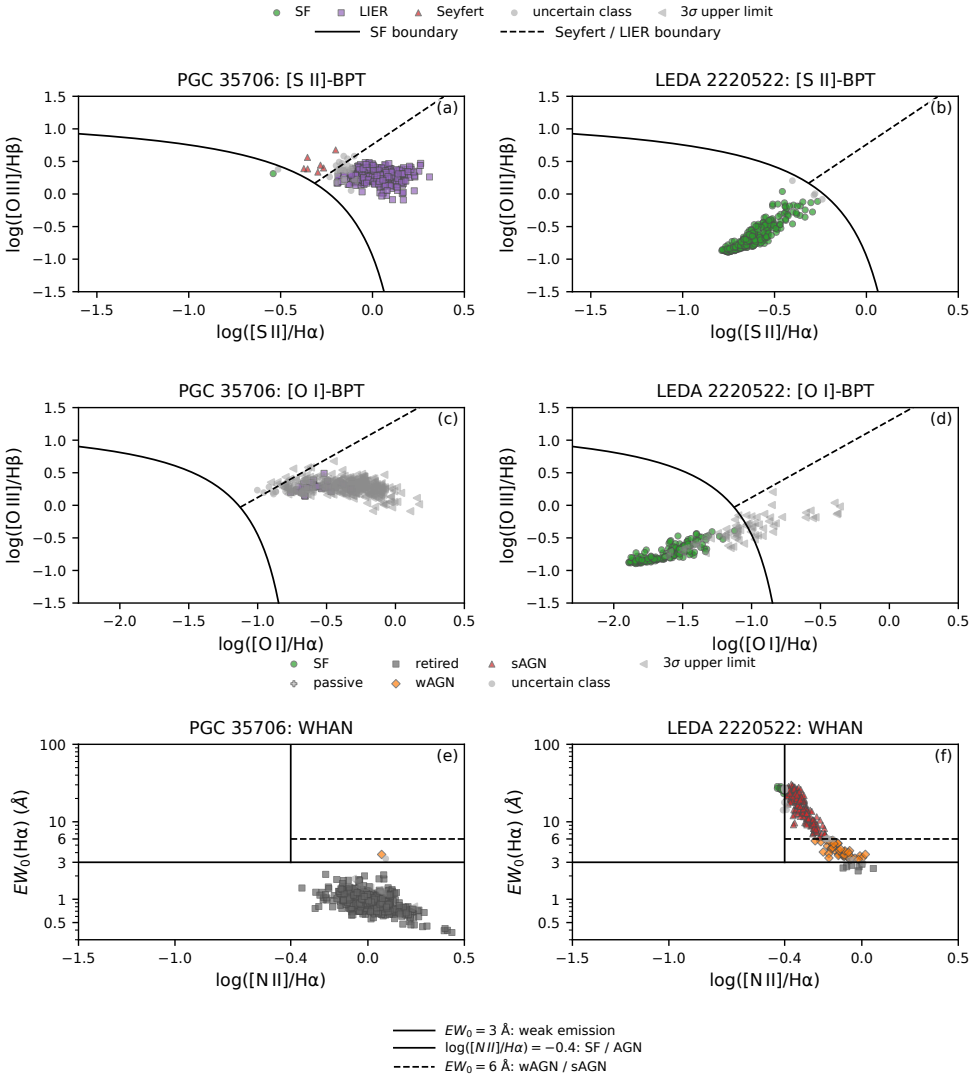


Figure 2 NBursts diagnostic diagrams for PGC 35706 (left) and LEDA 2220522 (right): [S II]-BPT (a,b), [O I]-BPT (c,d), and WHAN (e,f). Each point represents one spectral bin. On BPT diagrams, the solid curve bounds the star-forming (SF) region below and to the left, while the dashed line separates Seyfert excitation above from LIER excitation below. On WHAN, the dashed line separates wAGN and sAGN; the other boundaries are solid. For lines with $S/N < 3$, upper limits of $\max(F, 0) + 3\sigma_F$ are shown.

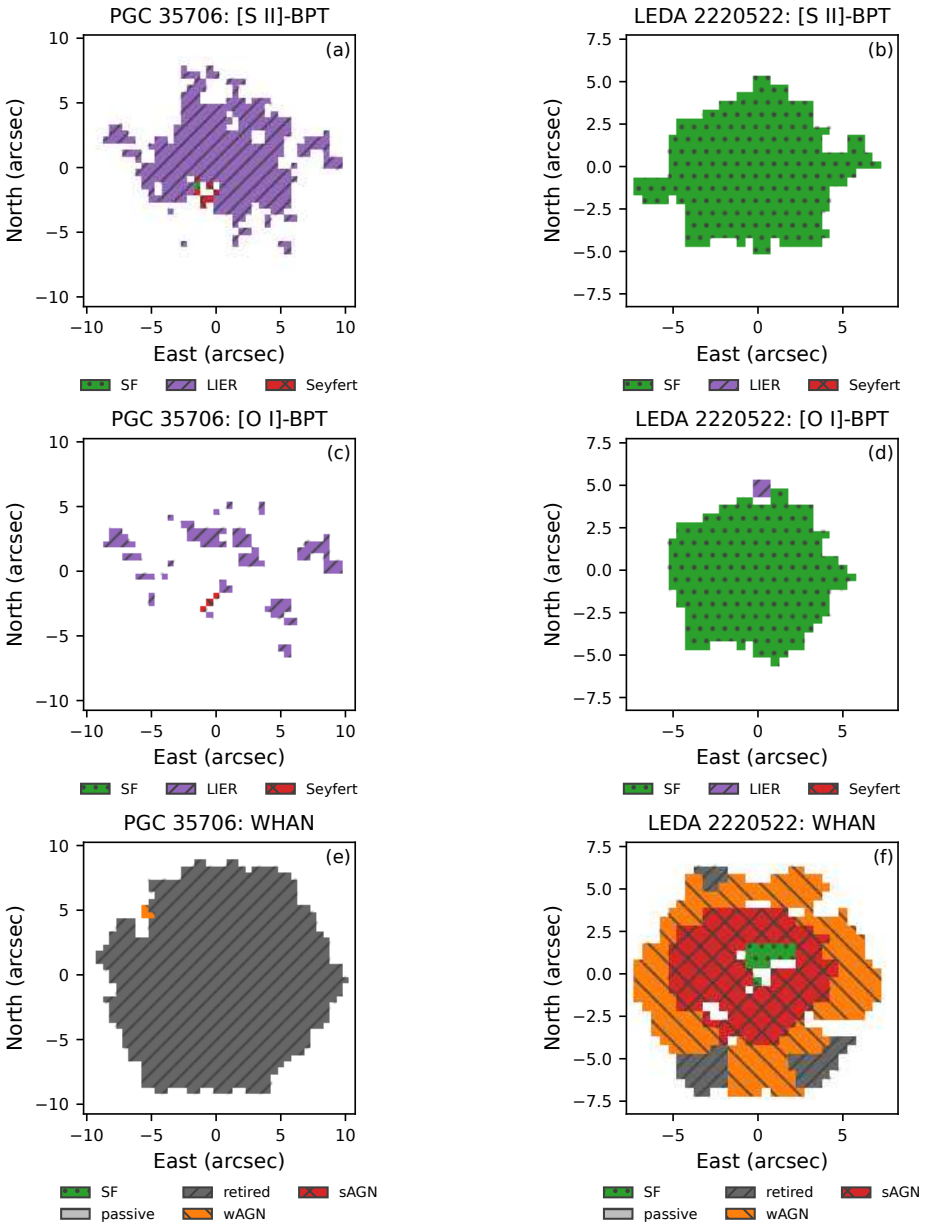


Figure 3 Spatial maps of the most probable NBursts classes for PGC 35706 (left column) and LEDA 2220522 (right column): [S II]-BPT (a,b), [O I]-BPT (c,d), and WHAN (e,f). A class is shown only when its probability is at least 0.8; white regions are unclassified or masked. Grey WHAN regions indicate the retired and passive sectors, distinguished by shading and hatching in the legend.

4.2 Comparison with DAP results

In PGC, the NBursts Hβ flux is approximately half the DAP value (Table 3), whereas Hα and [N II] are about 15 per cent higher and the median [O III] ratio is close to unity. The Hβ flux ratio persists in single-spaxel bins (0.527) and when $S/N \geq 10$ is required in both analyses (0.528). The discrepancy therefore cannot be reduced to binning or a weak signal. For a common sample of 350 bins, the median Hα/Hβ ratios are 2.65 from NBursts and 1.25 from DAP.

Table 3 Flux ratios $F_{\mathrm{NBursts}}/F_{\mathrm{DAP}}$ in identical apertures for lines detected at $S/N \geq 3$ in both original analyses. The median, 16th and 84th percentiles, and number of bins N are given for each line.

Line	PGC 35706	N	LEDA 2220522	N
Hα	1.152 [1.046; 1.326]	588	1.013 [1.006; 1.027]	230
Hβ	0.530 [0.366; 0.749]	350	0.935 [0.901; 0.975]	226
[O III]λ5007	1.001 [0.888; 1.140]	573	0.756 [0.689; 0.880]	221
[N II]λ6584	1.152 [1.075; 1.229]	586	1.000 [0.976; 1.013]	230
[S II]λ6717	1.032 [0.867; 1.207]	527	1.004 [0.973; 1.046]	227
[S II]λ6731	1.049 [0.858; 1.229]	485	1.030 [0.990; 1.077]	224
[O I]λ6300	0.405 [0.333; 0.655]	51	1.073 [0.873; 1.306]	158

In LEDA, median Hα, [N II], and [S II] fluxes agree to within a few per cent, while NBursts Hβ is about 7 per cent lower and [O III] 24 per cent lower. In the 226 common bins, the median Hα/Hβ ratios are 4.76 and 4.44, respectively.

On the common sample for each diagnostic, [N II]-BPT classes agree in 259 of 347 PGC bins (74.6 per cent) and 209 of 219 LEDA bins (95.4 per cent). Agreement is 294/305 and 217/217 for [S II]-BPT, and 583/585 and 221/230 for WHAN, respectively. In PGC, the [N II]-BPT classification is more sensitive to the spectral analysis than the WHAN classification of weak emission.

At the intersection of the two star-forming masks in LEDA, comprising 192 bins over 53.25 square arcseconds, the SFR is 1.116 $M_{\odot}\,\mathrm{yr}^{-1}$ from NBursts and 0.920 $M_{\odot}\,\mathrm{yr}^{-1}$ from DAP. The difference of about 21 per cent persists at fixed area. Over the same region, the median O3N2 estimates of $12 + \log(\mathrm{O/H})$ are 8.624 and 8.604: the difference of 0.020 dex is smaller than the adopted calibration scatter of 0.18 dex.

To assess the sensitivity of the SFR to the Hβ profile, we perform a local Gaussian fit with free amplitude, centre, width, and a linear residual continuum. The NBursts stellar model and Hα flux are fixed. This variant gives an SFR of 0.950 $M_{\odot}\,\mathrm{yr}^{-1}$ in the same 192 bins; varying the spectral-window half-width from 25 to 45 Å gives 0.947–0.955 $M_{\odot}\,\mathrm{yr}^{-1}$.

4.3 Gas and stellar kinematics

The axisymmetric model leaves structured residuals in PGC (Fig. 4), with a root-mean-square value of 45.5 $\mathrm{km\,s}^{-1}$. Nine peripheral bins with $|V - V_{\mathrm{mod}}| > 60$ $\mathrm{km\,s}^{-1}$ contribute 89.3 per cent of the sum of squared residuals, whereas a robust scatter estimate is 12.5 $\mathrm{km\,s}^{-1}$.

For LEDA, the root-mean-square residual is 5.90 $\mathrm{km\,s^{-1}}$ and remains small under the tested changes in selection and geometry. At the resolution of the observations, the field is consistent with regular rotation. Table 4 summarizes the fit diagnostics and sensitivity ranges.

The NBursts gas and stellar velocity gradients are nearly opposite in both galaxies. DAP reproduces the same large-scale direction of gas motion, but local agreement between the two gas-velocity estimates is substantially poorer in PGC than in LEDA (Fig. 5 and Table 4). Signed differences between the directed angles and their uncertainties are given in Table 5.

The Hα line widths corrected for instrumental broadening are larger in PGC (Table 4).

Table 4 Gas-kinematic diagnostics. Root-mean-square fit residuals are unweighted; sensitivity ranges cover changes in selection and geometry. The NBursts–DAP difference is calculated on common bins after separately subtracting the medians. Brackets for the line widths give spatial 16th and 84th percentiles.

Quantity	PGC 35706	LEDA 2220522
NBursts gas bins	631	263
Fit residual, rms ($\mathrm{km\,s^{-1}}$)	45.5	5.90
rms sensitivity range ($\mathrm{km\,s^{-1}}$)	44.4–57.7	5.73–5.92
Descriptive χ^2/ν	4.59	0.67
Degrees of freedom ν	625	257
Common NBursts–DAP bins	601	256
Pearson coefficient r	0.825	0.994
NBursts–DAP difference, rms ($\mathrm{km\,s^{-1}}$)	55.1	2.44
Spaxels in the DAP line-width map	535	378
Median DAP line width ($\mathrm{km\,s^{-1}}$)	69.7 [45.5–113.0]	31.8 [22.0–42.8]

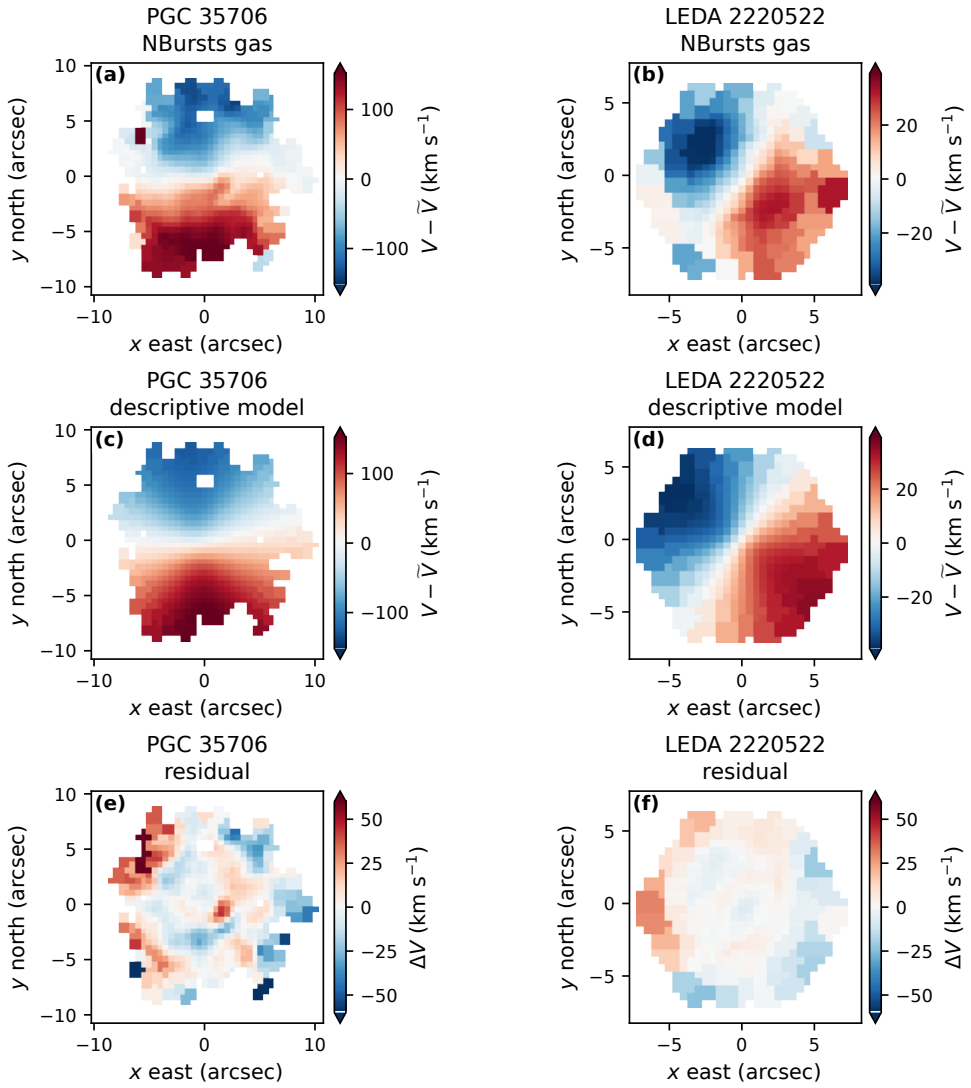


Figure 4 Observed NBursts ionized-gas velocity (a,b), axisymmetric model evaluated in Voronoi bins (c,d), and observed-minus-model residuals (e,f) for PGC 35706 (left) and LEDA 2220522 (right). Both residual maps span ± 60 km s^{-1}.

Table 5 Signed differences in velocity-gradient directions, in degrees, with angles measured from east towards north. Brackets give the 16th–84th percentile intervals of a spatial block bootstrap. Gas is compared with the model on NBursts gas bins.

Difference $\theta_A - \theta_B$	PGC 35706	LEDA 2220522
NBursts gas − stars	−176.5 [−179.7, −174.3]	−173.6 [−178.5, −169.8]
NBursts gas − DAP gas	0.34 [−1.27, 1.65]	1.14 [0.61, 1.63]
NBursts gas − retrograde model	3.9 [1.0, 6.2]	14.1 [11.9, 16.2]

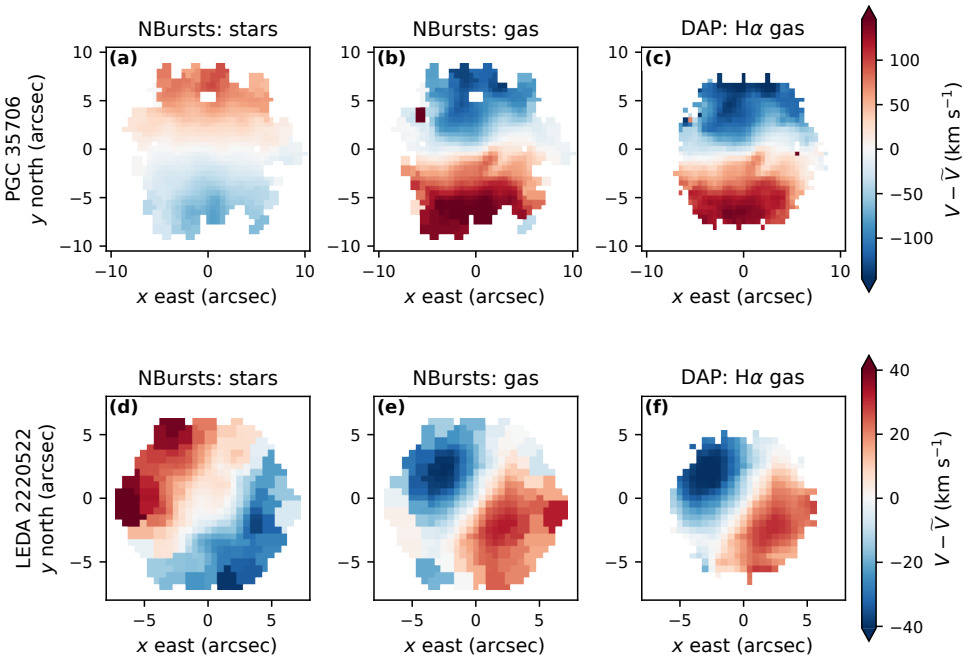


Figure 5 Integrated stellar velocity from NBursts (a,d), gas velocity from NBursts (b,e), and DAP Hα velocity (c,f) for PGC 35706 (top) and LEDA 2220522 (bottom). The median has been subtracted from each map. Each galaxy uses a common velocity scale limited to the 98th percentile of $|V - \widetilde{V}|$ over the combined elements of the three maps. NBursts maps show entire accepted bins; DAP maps show spaxels passing the quality cuts and $S/N(\mathrm{H}\alpha) \geq 3$ threshold.

4.4 Gas and model orbital families

The full stellar models reproduce the large-scale pattern of the observed stellar velocities, with Pearson correlation coefficients of $r = 0.986$ for PGC and 0.933 for LEDA.

The observed gas velocities correlate with the projected fields of the broad retrograde families, with $r = 0.856$ for PGC and 0.947 for LEDA (Figs. 6 and 7). The gradient directions differ by 3.9 and 14.1 deg, respectively (Table 5).

A local test of the relation between model orbit density and gas properties revealed no association that was robust to all the null models tested (Appendix B).

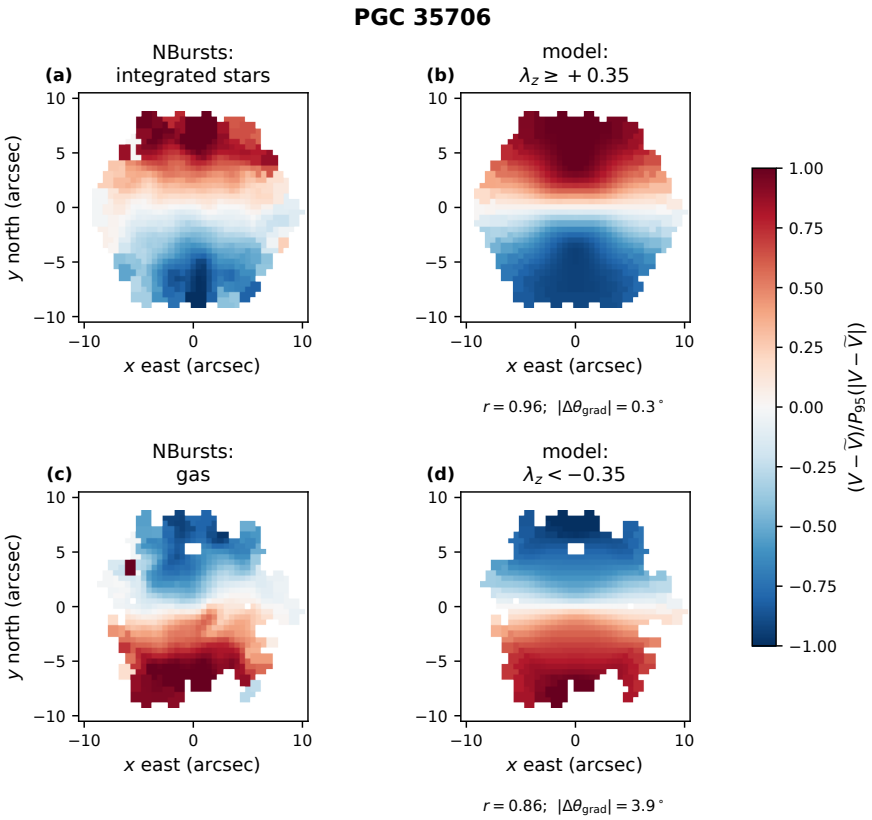


Figure 6 PGC 35706: observed integrated stellar velocity (a), projected velocity field of the broad prograde orbital family (b), observed gas velocity (c), and projected velocity field of the broad retrograde family (d). Each map shows $(V - \widetilde{V})/P_{95}(|V - \widetilde{V}|)$, clipped to $[-1, 1]$, where $\widetilde{V}$ and P_{95} are the median and 95th percentile for that map. Below the model maps, the correlation coefficient r and absolute difference in gradient directions are given for pairs (a,b) and (c,d).

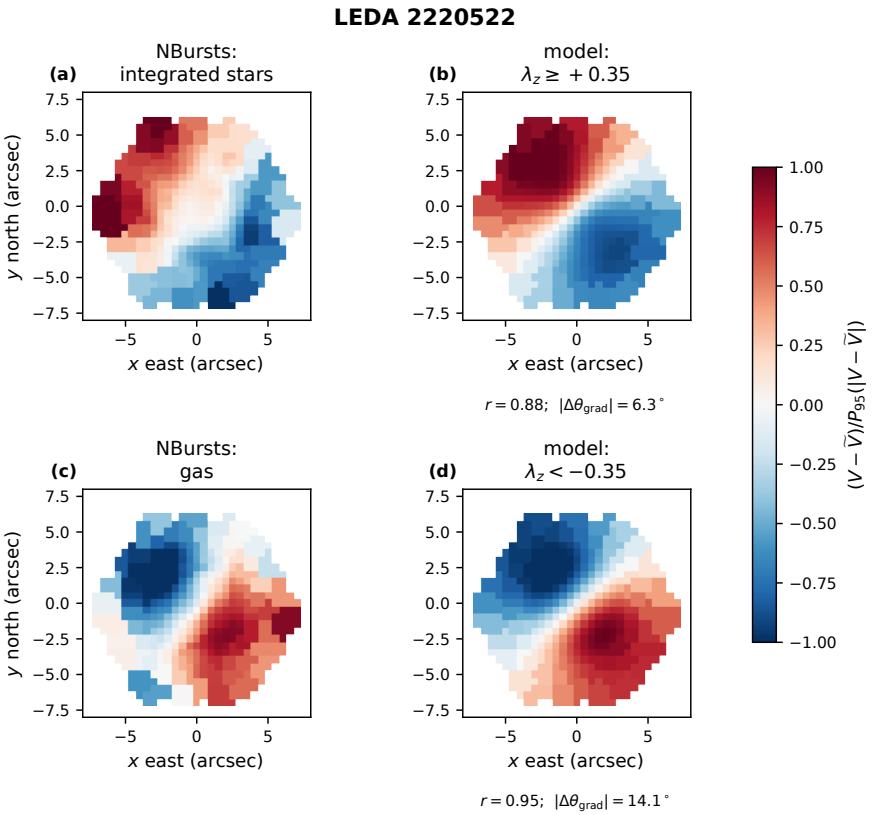


Figure 7 LEDA 2220522: observed integrated stellar velocity (a), projected velocity field of the broad prograde orbital family (b), observed gas velocity (c), and projected velocity field of the broad retrograde family (d). Normalization and panel pairs are as in Fig. 6.

5 Discussion

5.1 Gas-field regularity and excitation

In LEDA, the regular rotation model describes the gas field well. In PGC, it leaves structured residuals, with the large root-mean-square deviation driven by a few peripheral bins. PGC also differs from LEDA in having broader emission lines. Both the gas velocity dispersion and spatially unresolved velocity gradients contribute to the observed line width.

The contrast between these galaxies despite similar stellar–gas velocity-gradient angles shows why the spatial regularity of the field must be assessed alongside the gradient direction. In selecting regularly rotating gas, this criterion complements the position-angle threshold (Bao et al. 2022); disturbed and irregular systems also show greater gas-field asymmetry or uncertainty in the kinematic position angle (Zhou et al. 2022; Beom et al. 2024).

Excitation diagnostics reveal a second difference. LEDA contains regions with evidence of star formation, whereas the small $EW(\mathrm{H}\alpha)$ and WHAN classification in PGC are consistent with ionization by an old stellar population. Population studies likewise identify different ionization and star formation regimes among systems with misaligned stellar and gas motions (Ristea et al. 2022; Tous et al. 2026).

5.2 Sensitivity to spectral analysis

NBursts and DAP agree on the large-scale direction of gas motion and reproduce the excitation contrast between the galaxies. For LEDA, the main discrepancy in derived quantities arises from the Balmer lines: different Hβ fluxes change the internal-attenuation correction and the SFR estimate. The difference in SFR between the analyses substantially exceeds its formal statistical uncertainty, whereas the O/H estimates agree within the calibration scatter.

The large root-mean-square residual in PGC is driven by a few peripheral bins. In some of these bins, the measured velocities are sensitive to spectral fitting and quality cuts (Appendix A.3). The amplitude of the extreme deviations is therefore less robust to the spectral analysis than the direction of gas motion.

5.3 Formation scenarios

In LEDA, regular gas counterrotation and star-forming regions are consistent with external gas accretion followed by star formation (Katkov et al. 2013, 2016; Chen et al. 2016). Stellar-component ages and metallicities have already been estimated by Goradzhanov et al. (2026b). Testing the sequence of accretion and star formation requires models of the joint evolution of gas and stars over time, consistent with these estimates and the observed kinematics.

The projected similarity of the gas and retrograde stellar-family velocity fields provides an additional kinematic constraint on such evolutionary models.

6 Conclusions

1. LEDA has a comparatively regular ionized-gas velocity field. The axisymmetric model leaves small residuals, and NBursts and DAP gas velocities agree in both the large-scale gradient direction and individual bins. Regions consistent with star formation allow the SFR and oxygen abundance to be estimated within the selected part of the MaNGA coverage. The SFR estimate is sensitive to the analysis of the Balmer lines.
2. In PGC, nearly opposite large-scale gas and stellar velocity gradients coexist with structured model residuals and local discrepancies between the two gas-velocity estimates. The root-mean-square residual is dominated by a few peripheral bins with extreme values. The gas exhibits weak emission relative to the continuum, predominantly with low-ionization excitation on [S II]-BPT, in contrast to the star-forming regions in LEDA.
3. Gas velocities correlate with the projected velocity fields of broad retrograde orbital families in the stellar dynamical models.

Comparison of the two galaxies shows that nearly opposite stellar and gas velocity gradients must be interpreted in conjunction with the spatially resolved regularity of the velocity field and gas excitation.

Acknowledgements

This research was carried out within the framework of the state assignment of M. V. Lomonosov Moscow State University.

Appendix A Measurement details and sensitivity

A.1 Kinematic fitting and uncertainties

The arctangent model has six free parameters: $V_{\rm sys}$, the projected orientation, A, R_t, and two centre coordinates, each restricted to ± 2 arcsec. We use a soft L_1 loss for residuals divided by $\sigma_{\rm eff} = [\sigma_V^2 + (5\ {\rm km\,s^{-1}})^2]^{1/2}$. The root-mean-square residual is unweighted, and $\nu = N - 6$. The robust scatter estimate is $1.4826\,{\rm median}|r - {\rm median}(r)|$, where $r = V - V_{\rm mod}$. The reported χ^2/ν describes the residuals after this robust fit. Sensitivity tests vary the Hα threshold, central-region exclusion, and inclination. DAP line-width measurements require $S/N(\mathrm{H}\alpha) \geq 5$, valid widths, and a positive squared dispersion after the instrumental correction. The plane-gradient angle is $\theta_{\rm grad} = {\rm atan2}(b, a) \pmod{360^\circ}$. The corresponding standard astronomical position angle, measured from north towards east, is $(90^\circ - \theta_{\rm grad}) \pmod{360^\circ}$. For fields A and B, the signed difference is defined as $\delta\theta_{A-B} = {\rm wrap}_{[-180^\circ,180^\circ)}(\theta_A - \theta_B)$. Angular uncertainties are estimated from 2000 joint spatial block bootstrap samples. The same procedure is applied to DAP Hα velocities after Hα-flux-weighted averaging in common NBursts bins. In all maps, the x-axis points east and the y-axis north.

A.2 Emission-line classification and checks

For each bin, the flux normalization is set by the ratio of the integral of the isolated Hβ model over observed wavelength to its tabulated flux. The median factor is 1.077 for PGC and 1.075 for LEDA; integration of the Hα+[N II] complex gives a consistent normalization. The same factor is applied to flux uncertainties. The equivalent width is the ratio of this integrated flux to the continuum, divided by $1+z_{\rm line}$; EW uncertainties are scaled in the same way. The Milky Way correction is applied to fluxes but cancels in EW.

The original tables lack [O I] fluxes and uncertainties for 181 PGC bins and 20 LEDA bins. After subtracting the fixed stellar model from the spectrum, the residual is integrated within a window of half-width 6–14 Å, chosen according to the width of the neighbouring strong [N II] line. The centre is transferred from that line using the ratio of laboratory wavelengths. A linear residual continuum is estimated in sidebands 18–35 Å from the centre; the uncertainty includes spectral noise and continuum uncertainty, with inflation for excess scatter in the sidebands. Flux estimates are obtained for 179 and 20 bins; the remaining two PGC bins fail the basic Balmer-line selection. Negative estimates are retained as noisy measurements and are not replaced by zeros.

The WHAN diagram uses [N II]/Hα and EW(Hα) (Cid Fernandes et al. 2011). The retired sector corresponds to $EW(\mathrm{H}\alpha) < 3$ Å, except for the passive sector, which requires both $EW(\mathrm{H}\alpha) < 0.5$ Å and $EW([\mathrm{N\,II}]) < 0.5$ Å. At $\log([\mathrm{N\,II}]/\mathrm{H}\alpha) \geq -0.4$, the intervals $3 \leq EW(\mathrm{H}\alpha) < 6$ Å and $EW(\mathrm{H}\alpha) \geq 6$ Å are denoted wAGN and sAGN. The WHAN star-forming region additionally requires $\log([\mathrm{N\,II}]/\mathrm{H}\alpha) < -0.4$ and $EW(\mathrm{H}\alpha) \geq 3$ Å.

For [S II]- and [O I]-BPT diagrams (Baldwin et al. 1981; Kewley et al. 2001, 2006), the base mask requires valid Hα, Hβ, and [O III] measurements with $S/N \geq 3$ and valid flux uncertainties for the relevant weak lines. Fluxes are sampled from normal distributions truncated at zero; lines are treated as independent because their covariance is unavailable. The probabilistic WHAN classification uses Hα with $S/N \geq 3$, valid [N II] flux and both equivalent-width measurements, and a positive measured EW(Hα). The two fluxes and two equivalent widths are perturbed independently using the same non-negative error model. The joint [N II]-BPT/WHAN table classifies central measurement values on a common four-line detection mask. The ranges of fractions in that table are obtained by a spatial block bootstrap on the PSF scale. Each entire bin is assigned to a block according to its centre; in area weighting, its weight is the number of spaxels. Four grid origins are used. Neither these ranges nor the class probabilities include calibration uncertainties, systematic errors in continuum subtraction, or the unavailable covariances between lines and between fluxes and equivalent widths.

Both oxygen-abundance calibrations require $S/N \geq 3$ in Hβ, [O III], Hα, and [N II]. Their calibrated ranges are $-1.1 \leq$ O3N2 ≤ 1.7 and $-1.6 \leq$ N2 ≤ -0.2. The [N II]-BPT dividing curves are not extrapolated beyond their asymptotes.

To test the sensitivity of the PGC classification to a Balmer decrement below case B, we replace F(Hβ) with $\min[F(\mathrm{H}\beta), F(\mathrm{H}\alpha)/2.86]$. In this test, 97.5 per cent of the 319 bins with detected lines on [S II]-BPT and 91.8 per cent of the 49 bins on [O I]-BPT remain in the LIER sector; the rest lie in the Seyfert sector. No star-forming bins appear in these samples.

A.3 Control of spectral apertures and quality masks

To test the effects of spatial binning and quality selection, DAP version 3.1.0 is applied to 939 summed spectra on the NBursts tessellation, with the same fluxes, uncertainties, and base mask. Stellar kinematics are determined using the MILESHC library; the MaStarSSP weights and Gaussian gas profiles are then fitted with stellar kinematics held fixed. The standard additional DAP masks and instrumental-resolution treatment are used (Westfall et al. 2019; Belfiore et al. 2019). A common set of stellar templates is selected across the bins of each galaxy.

An additional cut excludes wavelengths at which at least one of the summed spaxels carries the DONOTUSE flag from the MaNGA Data Reduction Pipeline (DRP). It affects 112 PGC bins and 136 LEDA bins. Requiring at least 100 usable spectral samples leaves 618 PGC spectra and 233 LEDA spectra; 88 apertures are excluded. Both fitting stages are repeated for the retained spectra.

For the three measurement variants on the common sample, we fit the axisymmetric velocity-field model in Eq. 1 using the same inclinations, $S/N(\mathrm{H}\alpha) \geq 5$ threshold,

and error model. DAP velocities are converted to the logarithmic convention used by NBursts. Root-mean-square fit residuals are given in Table A1.

Table A1 Root-mean-square residuals of the axisymmetric gas-field model, in $\mathrm{km\,s^{-1}}$, for the common sample of 556 PGC apertures and 231 LEDA apertures.

Spectral measurements	PGC 35706	LEDA 2220522
NBursts	42.59	3.218
DAP: NBursts apertures	30.70	3.260
DAP: additional DRP mask	21.23	3.256

In LEDA, the root-mean-square residual is nearly identical for all three variants. In PGC, it decreases after the additional selection and DAP refitting, while the robust scatter estimate based on the median absolute deviation changes little (12.35 and 12.25 $\mathrm{km\,s^{-1}}$). The largest changes affect the extreme velocity measurements.

A.4 Sensitivity of the SFR and oxygen abundance in LEDA

The statistical SFR interval is obtained by Monte Carlo propagation of the measured Hα and Hβ flux uncertainties with the mask and attenuation law fixed. Standard-normal perturbations are shared by bins whose centres fall within the same 2.5 arcsec block, and are independent between blocks and between the two lines. The distributions are truncated at zero, and four grid origins are considered. The interval spans the 16th–84th percentiles and excludes uncertainty in mask selection and spectral-model systematics.

Table A2 compares additional restrictions on the primary LEDA mask. Formal detection of the weak lines tests sensitivity to fluxes near zero. The [N II]-BPT-SF and probabilistic WHAN-SF criteria select diagnostic subregions; their intersection contains 16 bins and has SFR $= 0.284\ M_\odot\,\mathrm{yr^{-1}}$.

Table A2 Sensitivity of the LEDA results to additional restrictions on the primary mask. N_{SFR} is the number of spectral bins; the last two columns give median oxygen abundances, with the number of valid estimates in parentheses. WHAN-SF denotes $P_{\mathrm{WHAN,SF}} \geq 0.8$. All estimates refer to the specified part of the MaNGA coverage.

Mask	N_{SFR}	SFR ($M_\odot\,\mathrm{yr^{-1}}$)	$12+\log(\mathrm{O/H})$ O3N2 (N_{cal})	$12+\log(\mathrm{O/H})$ N2 (N_{cal})
Primary probabilistic mask	203	1.124	8.622 (203)	8.588 (195)
Primary + all weak lines at $S/N \geq 3$	159	1.084	8.632 (159)	8.584 (159)
Primary + [N II]-BPT-SF	154	1.081	8.632 (154)	8.580 (154)
Primary + both preceding restrictions	141	1.065	8.633 (141)	8.580 (141)
Primary + [N II]-BPT-SF + WHAN-SF	16	0.284	8.634 (16)	8.551 (16)

With the primary mask fixed, a single correction based on the Balmer decrement of the summed fluxes gives 1.093 $M_\odot\,\mathrm{yr}^{-1}$. Summing the fluxes of entire bins in PSF-sized blocks before correcting for attenuation gives 1.102–1.108 $M_\odot\,\mathrm{yr}^{-1}$ for the four grid origins. Varying R_V from 2.5 to 4.0 gives 0.898–1.508 $M_\odot\,\mathrm{yr}^{-1}$.

Varying the window width used to recover missing [O I] measurements by 20 per cent in either direction does not change the primary mask. Applying the same direct [O I] measurement to all usable spectra gives 201 bins and SFR = 1.123 $M_\odot\,\mathrm{yr}^{-1}$. Repeating the random sampling for probabilistic classification preserves the primary mask; changing the probability threshold from 0.8 to 0.7 or 0.9 changes the SFR by less than 0.1 per cent. A local refit of the Hβ amplitude with the stellar spectrum and gas-line shape fixed gives 1.112 $M_\odot\,\mathrm{yr}^{-1}$ over the same region.

Appendix B Local relations between model orbit density and gas properties

An exploratory local test uses the projected surface density of model orbit weights with $\lambda_z < -0.7$. Cell weights are distributed uniformly over the spaxels of each Voronoi bin. Weights of cells that cross the circularity boundary are multiplied by the fraction of weight in strictly selected orbits within each radial cell. The map is smoothed with the MaNGA PSF and normalized to the total weight, then compared with gas properties on the PSF scale. For $EW(\mathrm{H}\alpha)$ and SF probability, the density is represented by its median within each spectral bin, and bins are grouped into spatial blocks according to their centre coordinates; at least two usable bins per block are required. For DAP line width and velocity residuals, we use the median map values within blocks.

We calculate partial Spearman correlations between the density of model orbit weights and each gas quantity, controlling for projected radius. The baseline two-sided permutation test shuffles gas values among blocks within three radial groups of equal size; four grid origins are tested. In LEDA, the line width corrected for instrumental broadening gives $\rho = 0.46$–0.64 and baseline $p = 0.0014$–0.040. This positive association is sensitive to the null model: permutations within five annuli give $p = 0.055$ for one grid origin, and the threshold calibrated with spatial correlations is exceeded for only three of the four origins. In this null model, line-width values are permuted according to the ranks of PSF-smoothed Gaussian noise within six radial groups of map elements. The detection is therefore not robust to all tested null models. For NBursts $EW(\mathrm{H}\alpha)$ in LEDA, the coefficient depends on the grid origin and ranges from -0.42 to 0.10; for [S II]-BPT SF probability, it ranges from -0.22 to 0.02. Neither association passes all four grid origins. No robust associations are found for the absolute velocity residual $|V - V_{\mathrm{mod}}|$ or for the PGC quantities either.

For NBursts quantities, an additional null model is constructed from independent Gaussian noise, smoothed with the PSF and averaged over spectral bins. Gas values are permuted according to the noise ranks within six radial quantile groups. A detection requires the absolute coefficient to exceed a separately calibrated boundary enclosing 95 per cent of the null distribution for all four grid origins. The confidence level of the boundary is 95 per cent. In independent null realizations, the frequency of joint exceedance did not exceed 0.75 per cent for the pairs considered.

References

Abdurro'uf, Accetta K, Aerts C, et al (2022) The seventeenth data release of the sloan digital sky surveys: Complete release of manga, mastar, and apogee-2 data. Astrophys. J. Suppl. Ser.259(2):35. https://doi.org/10.3847/1538-4365/ac4414

Algorry DG, Navarro JF, Abadi MG, et al (2014) Counterrotating stars in simulated galaxy discs. Monthly Notices of the Royal Astronomical Society 437:3596–3602. https://doi.org/10.1093/mnras/stt2154

Baldwin JA, Phillips MM, Terlevich R (1981) Classification parameters for the emission-line spectra of extragalactic objects. Publ. Astron. Soc. Pac.93:5–19. https://doi.org/10.1086/130766

Bao M, Chen Y, Zhu P, et al (2022) Different formation scenarios of counter-rotating stellar disks in nearby galaxies. The Astrophysical Journal Letters 926:L13. https://doi.org/10.3847/2041-8213/ac52ad, arXiv:2202.03848

Bao M, Chen Y, Yang M, et al (2024) Uncovering the formation of the counter-rotating stellar discs in sdss j074834.64+444117.8. Monthly Notices of the Royal Astronomical Society 528:2643–2652. https://doi.org/10.1093/mnras/stae243, arXiv:2401.11179

Bao M, Tang Z, Chen Y, et al (2026) Properties of galaxies with counter-rotating stellar disks in the manga survey. The Astrophysical Journal 1000:240. https://doi.org/10.3847/1538-4357/ae4ebb, arXiv:2603.04044

Belfiore F, Maiolino R, Maraston C, et al (2016) Sdss iv manga – spatially resolved diagnostic diagrams: a proof that many galaxies are liers. Mon. Not. R. Astron. Soc.461:3111–3134. https://doi.org/10.1093/mnras/stw1234

Belfiore F, Westfall KB, Schaefer A, et al (2019) The data analysis pipeline for the sdss-iv manga ifu galaxy survey: Emission-line modeling. Astron. J.158(4):160. https://doi.org/10.3847/1538-3881/ab3e4e

Beom M, Walterbos RAM, Bizyaev D (2024) Sdss. iv. manga: The impact of the acquisition of gas with opposite angular momentum on the evolution of galaxies. The Astronomical Journal 168:197. https://doi.org/10.3847/1538-3881/ad6f0b

Bevacqua D, Cappellari M, Pellegrini S (2022) Sdss-iv manga: integral-field kinematics and stellar population of a sample of galaxies with counter-rotating stellar discs selected from about 4000 galaxies. Monthly Notices of the Royal Astronomical Society 511:139–157. https://doi.org/10.1093/mnras/stab3732

Blanton MR, Bershady MA, Abolfathi B, et al (2017) Sloan digital sky survey iv: Mapping the milky way, nearby galaxies, and the distant universe. The Astronomical Journal 154:28. https://doi.org/10.3847/1538-3881/aa7567

Bugueño MC, Gómez FA, Dolfi A, et al (2026) Origins of coplanar counterrotating stellar disk components in late-type galaxies. i. identification, characterization, and formation mechanisms of coplanar counterrotating stellar disk components. Astron. Astrophys.707:A51. https://doi.org/10.1051/0004-6361/202557544, arXiv:2510.03106

Cardelli JA, Clayton GC, Mathis JS (1989) The relationship between infrared, optical, and ultraviolet extinction. Astrophys. J.345:245–256. https://doi.org/10.1086/167900

Chen YM, Shi Y, Tremonti CA, et al (2016) The growth of the central region by acquisition of counterrotating gas in star-forming galaxies. Nature Communications 7:13269. https://doi.org/10.1038/ncomms13269

Cid Fernandes R, Stasińska G, Mateus A, et al (2011) A comprehensive classification of galaxies in the sloan digital sky survey: how to tell true from fake agn? Mon. Not. R. Astron. Soc.413(3):1687–1699. https://doi.org/10.1111/j.1365-2966.2011.18244.x

Coccato L, Morelli L, Corsini EM, et al (2011) Dating the formation of the counter-rotating stellar disc in the spiral galaxy ngc 5719 by disentangling its stellar populations. Mon. Not. R. Astron. Soc.412:L113–L117. https://doi.org/10.1111/j.1745-3933.2011.01016.x

Coccato L, Morelli L, Pizzella A, et al (2013) Spectroscopic evidence of distinct stellar populations in the counter-rotating stellar disks of ngc 3593 and ngc 4550. Astron. Astrophys.549:A3. https://doi.org/10.1051/0004-6361/201220460

Coccato L, Fabricius M, Morelli L, et al (2015) Properties and formation mechanism of the stellar counter-rotating components in ngc 4191. Astronomy and Astrophysics 581:A65. https://doi.org/10.1051/0004-6361/201526560

Davis TA, Alatalo K, Sarzi M, et al (2011) The atlas3d project - x. on the origin of the molecular and ionised gas in early-type galaxies. Monthly Notices of the Royal Astronomical Society 417:882–899. https://doi.org/10.1111/j.1365-2966.2011.19355.x

Dey A, Schlegel DJ, Lang D, et al (2019) Overview of the desi legacy imaging surveys. Astron. J.157(5):168. https://doi.org/10.3847/1538-3881/ab089d

Gasymov D, Katkov IY, Rubtsov EV, et al (2025) Stellar corgi in manga: Stellar counterrotating galaxies identified in the manga survey. The Astrophysical Journal Supplement Series 281:19. https://doi.org/10.3847/1538-4365/ae0590, arXiv:2504.02925

Goradzhanov VS, Mishurin DD, Sil'chenko OK, et al (2026a) Dynamical modeling of kinematically decoupled galaxies: Structural components. Astrophysical Bulletin 81:407–423. https://doi.org/10.1134/S1990341326600328, arXiv:2608.28388

Goradzhanov VS, Parfenov KO, Mishurin DD, et al (2026b) Stellar population and dynamical modeling of galaxies with kinematically misaligned components: Age and metallicity of structural components. https://doi.org/10.48550/arXiv.2609.05216, arXiv:2609.05216

Hummer DG, Storey PJ (1987) Recombination-line intensities for hydrogenic ions. i. case b calculations for h i and he ii. Mon. Not. R. Astron. Soc.224(3):801–820. https://doi.org/10.1093/mnras/224.3.801

Johnston EJ, Merrifield MR, Aragón-Salamanca A, et al (2013) Disentangling the stellar populations in the counter-rotating disc galaxy ngc 4550. Mon. Not. R. Astron. Soc.428:1296–1302. https://doi.org/10.1093/mnras/sts121

Katkov IY, Sil'chenko OK, Afanasiev VL (2013) Lenticular galaxy ic 719: Current building of the counterrotating large-scale stellar disk. Astrophys. J.769:105. https://doi.org/10.1088/0004-637X/769/2/105

Katkov IY, Sil'chenko OK, Chilingarian IV, et al (2016) Stellar counter-rotation in lenticular galaxy ngc 448. Mon. Not. R. Astron. Soc.461:2068–2076. https://doi.org/10.1093/mnras/stw1452

Kauffmann G, Heckman TM, Tremonti C, et al (2003) The host galaxies of active galactic nuclei. Monthly Notices of the Royal Astronomical Society 346:1055–1077. https://doi.org/10.1111/j.1365-2966.2003.07154.x

Kennicutt JRobert C., Evans INeal J. (2012) Star formation in the milky way and nearby galaxies. Annu. Rev. Astron. Astrophys.50:531–608. https://doi.org/10.1146/annurev-astro-081811-125610

Kewley LJ, Dopita MA, Sutherland RS, et al (2001) Theoretical modeling of starburst galaxies. Astrophys. J.556(1):121–140. https://doi.org/10.1086/321545

Kewley LJ, Groves B, Kauffmann G, et al (2006) The host galaxies and classification of active galactic nuclei. Mon. Not. R. Astron. Soc.372(3):961–976. https://doi.org/10.1111/j.1365-2966.2006.10859.x

Khoperskov S, Zinchenko I, Avramov B, et al (2021) Extreme kinematic misalignment in illustristng galaxies: the origin, structure, and internal dynamics of galaxies with a large-scale counterrotation. Mon. Not. R. Astron. Soc.500(3):3870–3888. https://doi.org/10.1093/mnras/staa3330

Kroupa P (2001) On the variation of the initial mass function. Monthly Notices of the Royal Astronomical Society 322:231–246. https://doi.org/10.1046/j.1365-8711.2001.04022.x

Lacerda EAD, Cid Fernandes R, et al (2018) Diffuse ionized gas in galaxies across the hubble sequence at the califa resolution. Mon. Not. R. Astron. Soc.474:3727–3739. https://doi.org/10.1093/mnras/stx3022

Law DR, Cherinka B, Yan R, et al (2016) The data reduction pipeline for the sdss-iv manga ifu galaxy survey. The Astronomical Journal 152:83. https://doi.org/10.3847/0004-6256/152/4/83

Marino RA, Rosales-Ortega FF, Sánchez SF, et al (2013) The o3n2 and n2 abundance indicators revisited: improved metallicity calibrations based on califa and te-based literature data. Astron. Astrophys.559:A114. https://doi.org/10.1051/0004-6361/201321956

Martel H, Richard S (2020) Formation of counter-rotating stars during gas-rich disc–disc mergers. Mon. Not. R. Astron. Soc.498:940–958. https://doi.org/10.1093/mnras/staa2122

Morelli L, Pizzella A, Coccato L, et al (2017) Kinematic and stellar population properties of the counter-rotating components in the s0 galaxy ngc 1366. Astronomy and Astrophysics 600:A76. https://doi.org/10.1051/0004-6361/201630046

O'Donnell JE (1994) R(v)-dependent optical and near-ultraviolet extinction. Astrophys. J.422:158–163. https://doi.org/10.1086/173713

Ristea A, Cortese L, Fraser-McKelvie A, et al (2022) The sami galaxy survey: physical drivers of stellar–gas kinematic misalignments in the nearby universe. Monthly Notices of the Royal Astronomical Society 517:2677–2696. https://doi.org/10.1093/mnras/stac2839, arXiv:2210.01147

Rix HW, Franx M, Fisher D, et al (1992) Ngc 4550: A laboratory for testing galaxy formation. Astrophys. J. Lett.400:L5. https://doi.org/10.1086/186635

Rubin VC, Graham JA, Kenney JDP (1992) Cospatial counterrotating stellar disks in the virgo e7/s0 galaxy ngc 4550. Astrophys. J. Lett.394:L9. https://doi.org/10.1086/186460

Smee SA, Gunn JE, Uomoto A, et al (2013) The multi-object, fiber-fed spectrographs for the sloan digital sky survey and the baryon oscillation spectroscopic survey. The Astronomical Journal 146:32. https://doi.org/10.1088/0004-6256/146/2/32

Starkenburg TK, Sales LV, Genel S, et al (2019) On the origin of star-gas counterrotation in low-mass galaxies. Astrophys. J.878(2):143. https://doi.org/10.3847/1538-4357/ab2128

Thakar AR, Ryden BS (1996) Formation of massive counterrotating disks in spiral galaxies. Astrophys. J.461:55. https://doi.org/10.1086/177037

Tous JL, Raimundo SI, Riffel R, et al (2026) Fuelling the central region of galaxies with misaligned gas accretion. Monthly Notices of the Royal Astronomical Society 550:stag1385. https://doi.org/10.1093/mnras/stag1385, arXiv:2607.14823

Vasiliev E (2019) Agama: action-based galaxy modelling architecture. Monthly Notices of the Royal Astronomical Society 482:1525–1544. https://doi.org/10.1093/mnras/sty2672

Vasiliev E, Valluri M (2020) A new implementation of the schwarzschild method for constructing observationally driven dynamical models of galaxies of all morphological types. The Astrophysical Journal 889:39. https://doi.org/10.3847/1538-4357/ab5fe0

Westfall KB, Cappellari M, Bershady MA, et al (2019) The data analysis pipeline for the sdss-iv manga ifu galaxy survey: Overview. Astron. J.158(6):231. https://doi.org/10.3847/1538-3881/ab44a2

Zhang K, Yan R, Bundy K, et al (2017) Sdss-iv manga: the impact of diffuse ionized gas on emission-line ratios, interpretation of diagnostic diagrams and gas metallicity measurements. Mon. Not. R. Astron. Soc.466:3217–3243. https://doi.org/10.1093/mnras/stw3308

Zhou Y, Chen Y, Shi Y, et al (2022) Sdss-iv manga: global properties of kinematically misaligned galaxies. Monthly Notices of the Royal Astronomical Society 515:5081–5093. https://doi.org/10.1093/mnras/stac2016

Zinchenko IA (2023) Gas and stellar kinematic misalignment in manga galaxies: What is the origin of counter-rotating gas? Astronomy and Astrophysics 674:L7. https://doi.org/10.1051/0004-6361/202346846

Statements and Declarations

Funding. This research was carried out within the framework of the state assignment of M. V. Lomonosov Moscow State University.

Competing interests. The authors declare no competing interests.

Ethics approval. Not applicable.

Consent to participate. Not applicable.

Consent for publication. Not applicable.

Data availability. The primary MaNGA DR17 data products are publicly available at https://www.sdss4.org/dr17/manga/, and Legacy Surveys DR10 images at https://www.legacysurvey.org/dr10/. The derived classifications, measurements, kinematic fits, and model-comparison results are available from the corresponding author upon reasonable request.

Code availability. The analysis code is not publicly available.

Author contributions. D. Gasymov provided the NBursts full-spectrum fitting results. V. S. Goradzhanov and K. O. Parfenov designed this study and performed the new analysis, interpretation, visualization, and manuscript preparation. All authors reviewed and approved the final manuscript.